Reactive sites rich porous tubular yolk-shell g-C$_3$N$_4$ via precursor recrystallization mediated microstructure engineering for photoreduction

Na Tian[a], Ke Xiao[a], Yihe Zhang[a,*], Xingxu Lu[b], Liqun Ye[c], Puxian Gao[b], Tianyi Ma[d], Hongwei Huang[a,*]

[a] *Beijing Key Laboratory of Materials Utilization of Nonmetallic Minerals and Solid Wastes, National Laboratory of Mineral Materials, School of Materials Science and Technology, China University of Geosciences, Beijing 100083, China*
[b] *Department of Materials Science and Engineering & Institute of Materials Science, University of Connecticut, 97 N. Eagleville Road, Storrs, CT, USA*
[c] *Key Laboratory of Ecological Security for Water Source Region of Mid-line Project of South-to-North Water Diversion of Henan Province, College of Chemistry and Pharmaceutical Engineering, Nanyang Normal University, Nanyang, 473061, China*
[d] *School of Environmental & Life Sciences, The University of Newcastle (UON), Callaghan, NSW, 2308, Australia*

ARTICLE INFO

ABSTRACT

Photoabsorption, charge separation efficiency and surface reactive catalytic sites are three critical factors in semiconductor photocatalytic process, which determine the photocatalytic activity. For bulk g-C$_3$N$_4$ derived from direct pyrolysis of C/N rich precursors, reactive sites distributed on the lateral edges are very scarce. In this work, we report the template-free preparation of three novel structured g-C$_3$N$_4$, namely, porous tubular (PT) g-C$_3$N$_4$, porous tubular yolk-shell (PTYS) g-C$_3$N$_4$, and porous split yolk-shell (PSYS) g-C$_3$N$_4$, by an unprecedented precursor microstructure regulation of melamine crystals in a gas-pressure mediated re-crystallization process. Enhanced photoabsorption, increased surface area, largely improved separation and migration efficiencies of photoinduced charge carriers are simultaneously realized in these g-C$_3$N$_4$ structures. Noticeably, selective photo-deposition test uncovers that the porous outer-walls and inner-rods of PTYS g-C$_3$N$_4$ are enriched by abundant reductive reactive sites, which consumedly boost the photo-reduction activity. Collectively promoted by these advantages, PTYS g-C$_3$N$_4$ shows not only an efficient H$_2$ production activity with a high apparent quantum efficiency (AQE) of 11.8% at λ = 420 $\pm$ 15 nm, but also a superior CO$_2$ reduction for CO production than bulk g-C$_3$N$_4$ by a factor 5.6, which is verified by the ^{13}C isotopic labeling. This work develops precursor microstructure engineering as a promising strategy for rational design of unordinary g-C$_3$N$_4$ structure for renewable energy production.

1. Introduction

Graphitic carbon nitride (g-C$_3$N$_4$), as a metal-free and earth-abundant photocatalytic material, triggers worldwide research interests owing to the promising applications for water splitting, CO$_2$ reduction and selective synthesis, etc. [1–5]. It has a layered crystal structure with hydrogen bonds forming the basal planes and weak van der Waals forces between interlayers [6–8]. The photoexicited charge carriers prefer to transfer in the basal plane rather than across the interlayers due to the much larger electrostatic potential barrier perpendicular to the basal plane [9], which causes severe recombination of photoinduced electrons and holes in bulk g-C$_3$N$_4$. On the other hand, reactive sites as the key locations for surface catalytic reaction also take crucial part in photocatalytic redox process. The insufficient reactive sites of bulk g-C$_3$N$_4$ considerably restrict the overflow of charge carriers and adsorption of reactants, such as H$_2$O/H$^+$, CO$_2$, impeding the photocatalytic activity improvement. Developing efficacious strategies for disposing of the aforementioned issues consume a deluge of efforts, but with little avail so far.

Nanomaterials synthesis with various morphologies has achieved great triumph in the catalytic, electronic, and energy conversion fields over the past decade because of their appearance-dependent and tunable physicochemical properties [10–14]. Diversity of nanomaterials in size, morphology and microstructure lead to the differences in surface atomic arrangement, surface energy and interfacial effect, giving rising to distinct mechanical, optical, thermal, electronic and magnetic properties [15–18]. Hence, control on the microstructure and morphology is regarded as a promising tactic for optimizing the properties

of materials. Microstructure control has always been an important research direction of g-C$_3$N$_4$ in improving the photocatalytic performance. The as-reported versatile g-C$_3$N$_4$ from zero-dimensional (0D) quantum dots, 1D nanorods/nanotubes, 2D nanosheets to 3D (hollow) microspheres exhibit enlarged specific surface area, improved charge separation as well as abundant reactive sites, thus showing greatly boosted photocatalytic water splitting or CO$_2$ reduction performance [19–22]. In particular, the g-C$_3$N$_4$ nanorods/nanotubes allow the photogenerated charges to swiftly migration along the specific direction, which could realize the spatial charge separation. On the other hand, constructing porous structure in bulk g-C$_3$N$_4$, such as the interconnected mesopores, can facilitate the transport of charge carriers and prevent its recombination. Meanwhile, plenty of lateral edges of pore walls supply adequate reactive sites for photoreduction [23–28]. However, the above-mentioned unordinary nano-architecture or porous structure of g-C$_3$N$_4$ are mainly confined to template synthetic methods, normally hard-template or soft-template, with several given template agents, such as SiO$_2$ or polystyrene nano/microspheres. The templates are always needed to be removed by hazardous reagents, and this method is also hard to yield some novel or uncommon microstructure [29–31]. Recently, Guo et al reported the preparation of phosphorus-doped hexagonal tubular carbon nitride (P-TCN) through a phosphorus acid-aided hydrothermal self-assembly process followed by thermal treatment [24]. The tubular structure collects the advantages of enhancement of light scattering and active sites, improved electrical conductivity and reduced band gap. P-TCN thus exhibited a high H$_2$ evolution rate with an apparent quantum efficiency (AQE) of 5.86% at 420 nm. Our group synthesized horn-like hollow mesoporous ultrathin (HHMU) g-C$_3$N$_4$ tubes by forming a horn-like Br-containing intermediate with further decomposition transformation under co-pyrolysis of melamine and substantial NH$_4$Br [26]. With high surface area, enhanced charge separation, carrier density, and surface charge-transfer efficiency, the HHMU g-C$_3$N$_4$ tubes also exhibit outstanding photocatalytic performance for H$_2$ evolution. Therefore, it is highly meaningful for developing eco-friendly synthetic routes to obtain novel g-C$_3$N$_4$ nanostructures to enrich the morphology and to advance recognition of relationship between microstructure and photoactivity of g-C$_3$N$_4$.

In crystallography, recrystallization is a common and simple method for obtaining single crystals with regular shape or good crystallinity [32–34]. In hydrothermal reaction, the vapour pressure determines the crystal structure of as-crystallized products, and the pressure-alteration often results in the formation of a new crystalline phase [33,35]. In our previous work, orthorhombic-phase melamine was obtained by treating the monoclinic-phase melamine (commercial melamine) with urea solution in hydrothermal process [35], and this new precursor yields mesoporous g-C$_3$N$_4$ nanosheets after calcination. Urea here was decomposed into NH$_3$ and CO$_2$, which provides a high pressure to induce the crystalline-phase transformation and surface etching of melamine. Sparked by the crystallography theory and our as-obtained results, engineering the microstructure of melamine crystals may be feasible by controlling the pressure in recrystallization process, which may finally give rise to an advanced g-C$_3$N$_4$ material upon calcination treatment.

In this work, we report the controlled fabrication of three novel structured g-C$_3$N$_4$ photocatalysts, including the porous tubular (PT) g-C$_3$N$_4$ (CN-1), porous tubular yolk-shell (PTYS) g-C$_3$N$_4$ (CN-2), and porous split yolk-shell (PSYS) g-C$_3$N$_4$ (CN-3) via regulating the microstructure of precursor melamine crystals in a hydrothermal recrystallization process. Introduction of abundant urea in the reaction solution (over 0.8 mol/L) gives rise to regular hexagonal-prism structured orthorhombic-phase melamine crystals with good crystallinity, which yields the tubular g-C$_3$N$_4$ following by calcination, and different tubular structures are obtained with further controlling the urea concentration. The three types of g-C$_3$N$_4$ all exhibit enhanced photoabsorption, increased surface area, largely improved separation and

migration efficiencies of photoinduced charge carriers. In addition, both the porous outer-walls and inner cores of PTYS CN-2 are active sites for reductive reaction, which contribute to the photocatalytic activity. Impressively, PTYS CN-2 demonstrates a consumedly improved photocatalytic activity for H$_2$ production and CO$_2$ reduction into CO in comparison with the bulk g-C$_3$N$_4$. This strategy furnishes a new perspective into fabrication of novel-structured g-C$_3$N$_4$ with high photocatalytic performance in an alternative, template-free and eco-friendly way.

## 2. Experimental section

2.1. Sample preparation

All the reagents used were AR grade and without further purification. Bulk g-C$_3$N$_4$ was synthesized via calcination treatment of 5 g melamine in a corundum crucible with a cover. The crucible containing melamine was put into furnace and heated at 520 °C for 4 h. After cooling to room temperature, yellow product g-C$_3$N$_4$ was obtained. PTYS CN-2 was synthesized as follows: 4.76 g (0.08 mol) urea was dispersed in 50 mL deionized (DI) water (the concentration of urea solution is 1.6 mol/L), and then 0.5 g (0.004 mol) melamine was put into the above solution with stirring for 30 min to obtain a suspension. After that, the suspension was transferred into a Teflon-lined stainless autoclave (100 mL) and heated at 180 °C for 24 h in an oven. After cooling to room temperature naturally, the products were collected by filtration without washing by DI water, and then put in fume hood for 7 days. Followed by a same calcination process to that of bulk CN, the PTYS CN-2 was finally obtained. PT CN-1 and PSYS CN-3 were prepared with the same procedure only by changing the urea concentration (0.8 and 2.4 mol/L, respectively). The pre-CN-NH$_4$Cl, pre-CN-Na$_2$CO$_3$, pre-CN-NH$_4$HCO$_3$, and pre-CN-NaOH samples were obtained with the same procedure to pre-CN-2, only replacing the urea by NH$_4$Cl (4.28 g), Na$_2$CO$_3$ (4.24 g), NH$_4$HCO$_3$ (3.16 g), and NaOH solution (pH = 9).

2.2. Characterization

The powder X-ray diffractometer (XRD) patterns of samples were obtained on a Bruker D8 Focus X-ray diffractometer with Cu Kα radiation (λ = 1.5405 Å) with a 0.02°/s scanning rate. The Fourier transform infrared (FTIR) spectra of the samples were recorded on a Bruker spectrometer in the frequency range of 4000-450 cm^{-1}. Thermogravimetric analysis (TGA) was performed on a Labsys TGDTA16 (SETARAM) thermal analyzer. Scanning electron microscopic (SEM) images were taken on an Auriga Zeiss FIB scanning electron microscope (SEM). The transmission electron microscroscope (TEM) images were obtained by a JEOL JEM-2010 F TEM operated at an accelerate voltage of 200 kV. The fluorescence micrographs were analyzed by Laser Scanning Confocal Microscope (Zeiss LSM780, Germany). UV–vis diffuse reflectance spectra (DRS) were measured by a Varian Cary 5000 UV–vis spectrophotometer. X-ray photoelectron spectroscopy with Al Ka X-rays (ht = 1486.6 eV) irradiation was operated at 150 W (XPS: Thermo ESCALAB 250, USA) was used to study the surface properties of the samples. The spectra were recorded at room temperature in air ranged from 370 nm to 700 nm. N$_2$ adsorption-desorption isotherms and pore-size distributions were recorded by a Quadrasorb SI MP apparatus at 77 K and the specific surface area of the samples was calculated using the Brunauer-Emmett-Teller (BET) method. The CO$_2$ absorption test was conducted on an specific surface and aperture analyser (ASAP2020, Micromeritics Instrument Corp., USA) at temperature of 30 °C. The surface photovoltage (SPV) tests were managed with a home-built apparatus, which combined with a lock-in amplifier (SR830) and a light chopper (SR540).
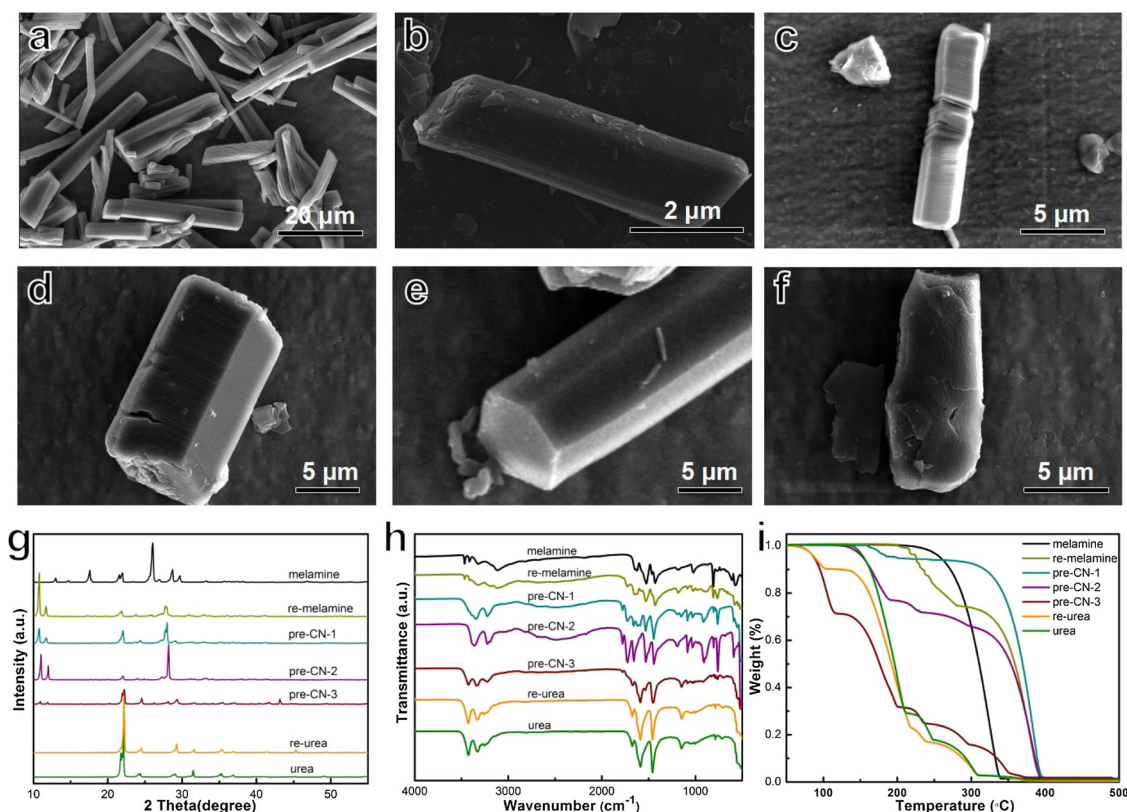
Fig. 1. SEM images of a, b) re-crystallized melamine treated by urea solution with urea:melamine molar ratio of 20:1 (pre-CN-2). Re-crystallized melamine treated by c) NH_4Cl, d) $NaHCO_3$, e) NH_4HCO_3 and f) NaOH solutions. g) XRD patterns, h) FTIR spectra and i) TGA curves of raw melamine, raw urea, hydrothermally treated pure urea (re-urea), hydrothermally treated pure melamine (re-melamine), and re-crystallized melamine treated by urea solution with urea:melamine molar ratio of 10:1, 20:1 and 30:1 (pre-CN-1, pre-CN-2 and pre-CN-3, respectively).

2.3. Photocatalytic H_2 evolution

The photocatalytic H_2 evolution tests were performed in a 150 mL quartz reactor at room temperature and vacuum pressure. The visible light was provided by a Xe-lamp (300 W) with a UV-cut off filter ($\lambda > 420$ nm). Typically, 50 mg of photocatalyst was suspended in 100 mL of aqueous solution containing 20% lactic acid scavenger in volume. The loading of 1 wt% Pt co-catalyst was conducted by directly dissolving H_2PtCl_6 into the above 100 mL mixed solution. Next, the suspensions were stirred and followed by illumination for 1 h at room temperature. Before the photocatalytic H_2 evolution reaction, co-catalyst suspensions were dispersed in an ultrasonic bath and nitrogen gas was bubbled through the reaction mixture for 30 min to remove the dissolved oxygen and to ensure the anaerobic conditions in the reaction system. The photocatalytic H_2 production experiments were measured on an online photocatalytic reaction system (Labsolar-AG, Beijing Perfect light Technology Co., Ltd China). At the given time intervals (1 h), hydrogen was analyzed by a gas chromatograph (GC7900, Tianmei, Shanghai, TCD, nitrogen as a carrier gas and 5 Å molecular sieve column). The procedure of photocatalytic H_2 generation of samples without loading Pt as co-catalyst was similar to the above process.

2.4. Photocatalytic CO_2 reduction

The photocatalytic CO_2 reduction experiment was carried out in a home-made closed gas system. In the reaction system, 0.1 g of photocatalyst was uniformly dispersed onto the watch-glass with an area of ~28 cm^2, which was then put in the reaction cell (Pyrex glass) with a total volume of 350 mL. Prior to the light irradiation, the above system was thoroughly vacuum-treated to completely remove air. After that, supercritical fluid-grade CO_2 gas (Minghui technical gases, Wuhan,

China) was introduced into the reactor until the pressure was 1 atm, and then 1 mL of DI water was injected into the reactor as the reductant, which was then kept for 30 min to establish an adsorption-desorption balance. After that, the reactor was irradiated from the top by 300 W Xe-lamp (PLS-SXE300. Beijing Perfect light Technology Co., Ltd China), and the photoreaction temperature was kept at 20 °C. During the irradiation, about 0.25 mL of gas was taken from the reaction cell for subsequent qualitative analysis by using SP 6800 A gas chromatography (GC) equipped with flame ionization detector (GC-FID, GDX-502 columns) and thermal conductivity detector (GC-TCD, TDX-01 columns). The quantification of the production yield was based on a calibration curve. The outlet gases were determined to be CO, O_2 and CO_2 but no CH_4, H_2 or other hydrocarbons. ^{13}C isotoptic labeling was employed to trace the carbon source. To confirm the origin of the as-produced CO, the isotopic $^{13}CO_2$ as feedstock for the photoreduction was conducted at room temperature with Ar as the carrying gas. A Pfeiffer OmniStar gas analysis mass spectrometer (Germany) was employed to analyze the products of the $^{13}CO_2$ isotopic experiment.

2.5. Photoelectrochemical measurements

Photoelectrochemical measurements were performed on an electrochemical analyzer (CHI660E, CHI Shanghai, Inc.) in a standard three-electrode configuration with a Pt wire as the counter electrode and Hg/Hg_2Cl_2 (in saturated KCl) as the reference electrode. Irradiation was proceeded with a Xe-lamp. Na_2SO_4 (0.1 M) aqueous solution was used as the electrolyte. The typical working electrode was prepared as follows: 10 mg ground sample was mixed with 1 mL alcohol to make slurry. The slurry was then dispersed onto a 2 cm × 4 cm ITO glass and then the ITO glass was dried at 60 °C for 10 h to obtain the working electrode.

3. Results and discussions

g-C_3N_4 prepared by direct calcination of the precursor melamine always shows bulky structure, which allows it insufficient reactive sites (Fig. S1) [9]. From the SEM image of melamine, the bulky structure of g-C_3N_4 is speculated to be ascribed to the block morphology of melamine (Fig. S2). As revealed in our previous work (described in the introduction part), hydrothermal treatment for melamine with low-concentration urea solution can cause its phase transformation, and the surface of melamine was etched by the gases from urea decomposition, finally yielding ultrathin g-C_3N_4 nanosheets after thermolysis. Herein, we introduce high concentrations of urea solution (0.8, 1.6, 2.4 mol/L) in the hydrothermal process of melamine, and explore the impact of larger vapour pressure resulted by more gases on morphology of the precursor melamine. As demonstrated by Figs. 1a–b, S3 and S4, melamine after hydrothermal recrystallization with urea concentrations of 0.8, 1.6 and 2.4 mol/L, namely pre-CN-1, pre-CN-2, and pre-CN-3, all show a hexagonal prismatic morphology. In contrast, the morphology of re-crystallized melamine and urea show not any noticeable change in the absence of urea in the hydrothermal process (Figs. S5 and S6). Thus, it is conjectured that the large vapour pressure of NH_3 and CO_2 from urea may be the main reason for the formation of melamine hexagonal prisms. To confirm the effect of as-decomposed gases on the morphology of recrystallized melamine, other chemicals that can decompose into gases when heating, such as NH_4Cl, $NaHCO_3$ and NH_4CO_3 were introduced for replacing urea. Interestingly, one can observe that similar hexagonal prisms also appear after hydrothermal treatment of melamine in the presence NH_4Cl, $NaHCO_3$ and NH_4CO_3 (Fig. 1c–e). However, after changing these decomposable salts to NaOH, irregular melamine crystals are observed (Fig. 1f), which implies that the pressure derived from gases (NH_3 and CO_2, Table S1) leads to the formation of hexagonal prisms morphology of recrystallized melamine.

For the hydrothermal treatment stage, melamine was transformed from monoclinic phase to orthorhombic phase regardless of whether urea was added (Fig. 1g), while the crystalline phase of urea remained the same before and after the hydrothermal process. The XRD patterns of pre-CN-1 and pre-CN-2 are well indexed into that of re-crystallized melamine (orthorhombic phase), indicating that pre-CN-1 and pre-CN-2 do not contain urea or re-urea. While the XRD pattern of pre-CN-3 is almost the same as that of urea/re-urea, which means that urea is the main component of pre-CN-3. It is concluded that the relatively high concentration (2.4 mol/L) of urea makes it easy to be isolated from solution. The conclusion of FTIR spectra (Fig. 1g) is the same as that of XRD patterns. Fig. 1i shows the TGA curves of raw melamine, raw urea, re-urea, re-melamine, pre-CN-1, pre-CN-2 and pre-CN-3. The thermal polymerization temperature of melamine is about 340 °C, while re-melamine, pre-CN-1 and pre-CN-2 completely decomposes at 400 °C, indicating that the crystalline phase of the latter three is the same but distinct from melamine. The urea and re-urea have the same decomposition temperature at 325 °C. As the decomposition temperature of pre-CN-3 is located between that of urea and re-melamine, it can be concluded that pre-CN-3 contains both re-melamine and urea, further verifying the conclusion from XRD and providing more detailed information for the phase transformation.

Inspired by the unique morphology of precursors, the microstructure of the product g-C_3N_4 was investigated. Interestingly, CN-1, CN-2 and CN-3 obtained separately from pre-CN-1, pre-CN-2 and pre-CN-3 all show tubular structure but with some differences (Figs. 2, S7–S9), and there are numerous mesopores on the tube wall (inset of Fig. 2g). Specifically, the CN-1 products are composed of uniform porous tubes (PT, Fig. 2a, d, g)). In contrast, CN-2 shows porous tubular yolk-shell (PTYS, Fig. 2b, e, h) structure, and there are inner-rods attached tightly to the inside of the hexagonal-prismatic porous tube shell. CN-3 shows similar morphology to CN-2, but most of the tube shells are split. Thus, it was denoted as porous split yolk-shell (PSYS) g-C_3N_4. The inner rods are comprised of numerous mesoporous

nanosheets (Fig. 2i), which may be beneficial for enhancing the specific surface area and harvesting more light. The fluorescence micrographs of CN-*x* (*x* = 1–3) also confirm their morphologies observed from above SEM and TEM images (Fig. S7). It is obvious to see that the tube shell easily bursts during the pyrolysis stage when adding a larger amount of urea in the hydrothermal process (like CN-3; Fig. 2c, f, i, l), which may be due to more gases emitted from decomposition of urea. However, when the same amounts of mechanically-mixed raw melamine and raw urea are employed as precursors, irregular sheet-like g-C_3N_4 products are obtained instead (Fig. S10). Therefore, the urea solution assisted hydrothermally treated process is an essential and critical step in formation of the final tubular structure of CN-*x* (*x* = 1–3).

Based on the above results, the formation mechanism for the various morphologies of g-C_3N_4 is tentatively proposed as illustrated in Scheme 1. Firstly, melamine was added in the urea solution, and then urea was decomposed into CO_2 and NH_3 during the hydrothermal process, resulting in a high vapour pressure in the autoclave (Table S1). Then, hexagonal-prism shaped melamine (pre-CN-1, pre-CN-2) and mixture of melamine and urea (pre-CN-3) were recrystallized when the molar ratios of urea:melamine were equal to 10:1, 20:1, and 30:1, respectively. After calcination of pre-CN-1, pre-CN-2 and pre-CN-3, PT CN-1, PTYS CN-2 and PSYS CN-3 were obtained. The difference between PT CN-1 and PTYS CN-2 may be due to the different crystallinity of pre-CN-2 and pre-CN-1 which is derived from the different vapour pressures in the hydrothermal stage, as demonstrated by slightly difference in their XRD patterns, FTIR spectra and TGA curves (Fig. 1g–i). As pre-CN-3 contains a large amount of urea, the fragmentation of CN-3 tube wall should be resulted from the high volume of gases (NH_3 and CO_2) released from urea in the thermal polymerization process.

The structure of the CN-*x* samples was investigated by XRD and FTIR. The XRD patterns of CN-1, CN-2, and CN-3 exhibit two typical diffraction peaks at 13.01° and 27.41°, corresponding to the in-plane structural packing and interfacial stacking of pristine g-C_3N_4, respectively (Fig. S11). Compared with pure g-C_3N_4, there is no change in the position of the characteristic peaks in the patterns of CN-*x*, indicating that CN-*x* maintains the original crystal structure of g-C_3N_4. However, both characteristic peaks were broadened and decreased in intensity with the addition of urea, suggesting that the hydrothermal pre-treatment process lowers the crystallinity of g-C_3N_4 and may cause the presence of nanostructure [35], which was confirmed by the following specific surface area measurement. From the FTIR spectra (Fig. S12), the absorption bands of the pure g-C_3N_4 sample indicate the typical molecular structure of g-C_3N_4. The intense bands located in the region of 1128–1634 cm^{-1} are assigned to the typical stretching modes of heterocyclic g-C_3N_4. The intense band at 807 cm^{-1} represents the out-of-plane breathing vibration characteristic of triazine units [36–38]. Peaks at 3068 and 3173 cm^{-1} are attributed to N—H stretching modes of residual nitrogen precursor species. In addition, the existence of peak at 3294 cm^{-1} is due to the existence of adsorbed water. No obvious differences in the diffraction peaks were detected, in line with the above XRD results, indicating that the as-prepared CN-*x* samples have the same chemical bonding as the bulk g-C_3N_4. The chemical composition of PTYS CN-2 was surveyed by XPS (Fig. S13). The N 1*s* spectrum can be deconvolved into three peaks with binding energies of 400.1 eV (N—H), 398.8 eV (three-coordinated N atoms, N_{3c}), and 397.8 eV (two-coordinated N atoms, N_{2c}) [39,40]. From Fig. S13, pure g-C_3N_4 sample has a typical N 1*s* spectrum, while for CN-2, the three peaks show a slight shift towards higher binding energy. Nevertheless, the relative position of the three peaks with respect to each other is the same as that for pure g-C_3N_4 sample [41,42]. The binding-energy difference of CN-2 between the N_{2c} peak and N_{3c} peak is approximately 1.3 eV, which is similar to that of pristine g-C_3N_4 (1.3 eV), elucidating that the main skeleton of g-C_3N_4 remains unchanged. However, the binding-energy gap from the N_{3c} peak to the N—H peak is approximately 1.1 eV, higher than that of pristine g-C_3N_4 (1.0 eV), suggesting a larger amount of nitrogen atoms on the surface of g-C_3N_4. Moreover, the organic
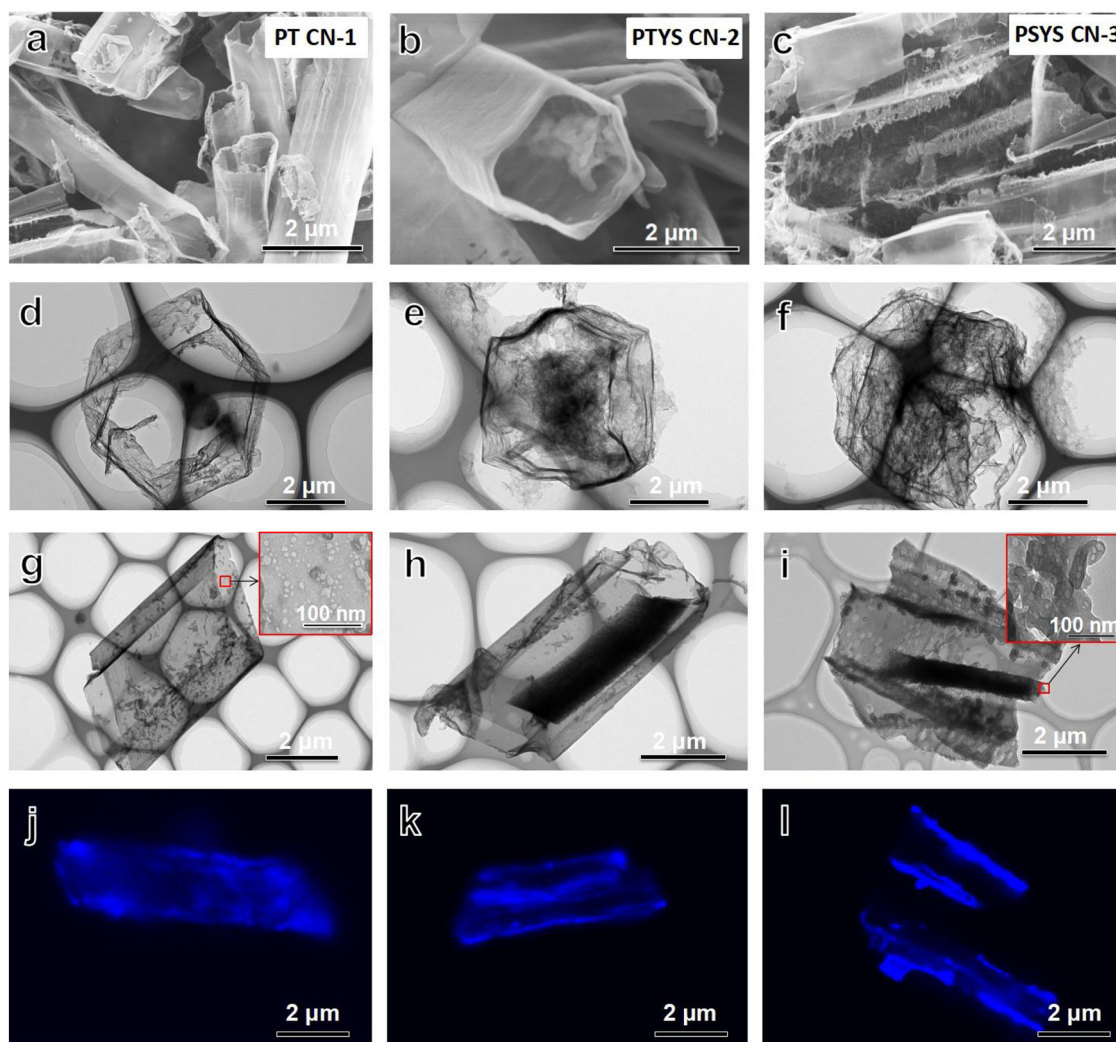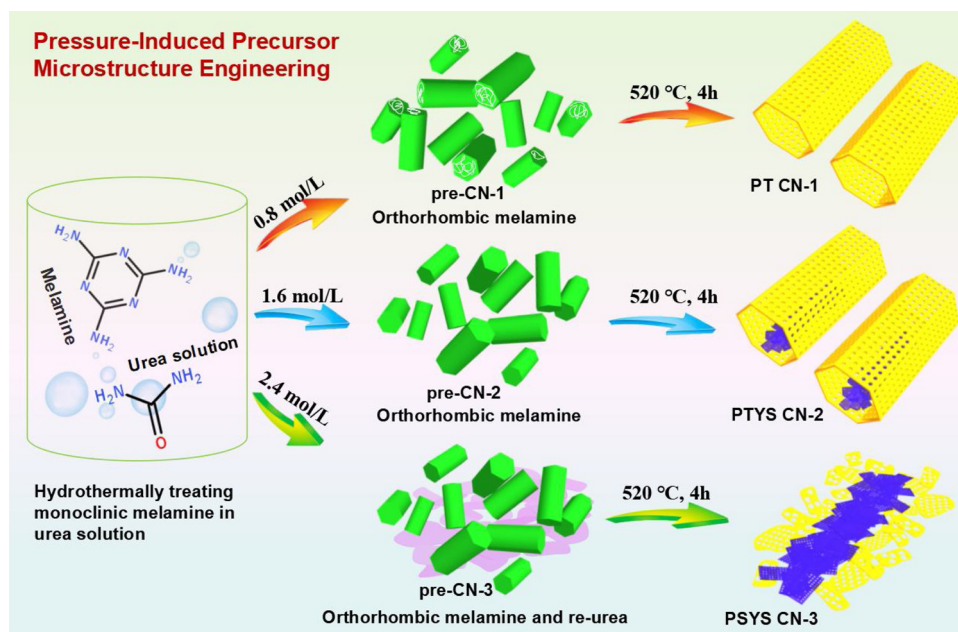
Fig. 2. SEM, TEM images and Fluorescence micrographs of (a, d, g, j) PT CN-1; (b, e, h, k) PTYS CN-2; (c, f, i, l) PSYS CN-3.

Scheme 1. Schematic illustration of the formation of CN-x (x = 1–3).

elemental analysis indicates that the N/C ratios in CN-x is higher than g-C$_3$N$_4$, and shows a gradual increase from CN-1 to CN-3 (Table S2), demonstrating the nitrogen doping in g-C$_3$N$_4$, consistent with our previous report [25].

The N$_2$ adsorption-desorption isotherms of CN-x samples are recorded, and these isotherms exhibit hysteresis loops, reflecting the presence of mesopores (Fig. S14a) [43]. The pore-size distribution curves of CN-x (Fig. S14b) show uniform mesopores with pore size of approximately 40 nm, which is consistent with the observation from TEM images (Fig. 2g, h, j). Owing to the appearance of porous tube and inner rod, CN-1 (24.63 m^2/g), CN-2 (41.02 m^2/g) and CN-3 (74.93 m^2/ g) show much higher specific surface area than bulk g-C$_3$N$_4$ (9.04 m^2/ g), and CN-3 possesses the largest specific surface area as a result of fragmented structure (Table S2). The optical properties of the CN-x were analyzed by ultraviolet-visible (UV–vis) absorption spectra (Fig. S15a). Obviously, CN-x samples display enhanced light absorption compared to pure g-C$_3$N$_4$ over the entire wavelength range, which is due to the porous and tubular structure with large surface area and multiple scattering effects [44,45]. The narrower band gaps of CN-x samples than pure g-C$_3$N$_4$ allow utilization of more solar spectrum to generate more photogenerated electron-hole pairs under visible light illumination (Fig. S15b).

The photocatalytic performance of bulk g-C$_3$N$_4$ and CN-x was evaluated by H$_2$ evolution and CO$_2$ reduction. Under visible light (λ > 420 nm) irradiation, CN-x samples all exhibit higher photocatalytic H$_2$ evolution activity than bulk g-C$_3$N$_4$, and the H$_2$ production rate of bulk g-C$_3$N$_4$, PT CN-1, PTYS CN-2 and PSYS CN-3 is 123 μmol h^{-1} g^{-1}, 247 μmol h^{-1} g^{-1}, 740 μmol h^{-1} g^{-1} and 390 μmol h^{-1} g^{-1}, respectively (Fig. 3a and b). The optimum photocatalytic H$_2$ production rate obtained for PTYS CN-2, increased by a factor of approximately 6 in comparison to bulk g-C$_3$N$_4$. These results clearly demonstrate that construction of tubular structure is an effective approach to improving the photocatalytic activity for g-C$_3$N$_4$, and the fine tubular yolk-shell structure is most beneficial to the photocatalytic activity enhancement. The photocatalytic H$_2$ evolution rate of CN-2 under different monochromatic light wavelengths (λ = 400, 420, 450, 500, 550 nm) well matches its DRS spectrum (Fig. 3c), confirming that the H$_2$ evolution was exclusively resulted from the photocatalytic activity of CN-2. In addition, PTYS CN-2 casts a high H$_2$ evolution AQE of 11.8% at 420 nm, which rivals most of reported porous or tubular g-C$_3$N$_4$ (Table S3). To exclude the possibility that the enhancement of H$_2$ evolution activity was resulted by Pt loading, a series of H$_2$ production experiments are conducted in the absence of Pt under the same test conditions. The H$_2$ evolution rate of CN-1, CN-2 and CN-3 shows the increase by 1.9, 3.7 and 2.4 folds compared to the pure g-C$_3$N$_4$ (Fig. S16), which is consistent with results of that with Pt loading. It indicates that the improved photocatalytic H$_2$ production originates from the change in microstructure of g-C$_3$N$_4$. Further, it is noteworthy that the unique morphology of CN-2 retained after four cycles of H$_2$ evolution experiment (Fig. 3d), confirming the good durability of the CN-2 photocatalyst. No substantial changes were observed in the XRD patterns of CN-2 sample after four successive cycles (Fig. S17), further demonstrating the high stability of the PTYS CN-2 photocatalyst.

The photocatalytic CO$_2$ reduction activity of the prepared photocatalysts were evaluated with illumination of a 300 W Xe lamp, and the results are shown in Fig. 3e. Similar to the trend of H$_2$ evolution, all the CN-x samples demonstrate higher CO$_2$ reduction activity for CO production, and the optimal performance was still obtained for PTYS CN-2 with a CO yield of 40.3 μmol g^{-1} within 4 h, which is about 5.6 times higher than that of pristine g-C$_3$N$_4$ (7.2 μmol g^{-1}). Blank experiment demonstrated that no CO product was detected without photocatalyst. The ^{13}C isotopic labeling experiment was conducted to verify the carbon source of the produced CO. As shown in Fig. 3f, the peaks at 2.3 min and m/z 29 are assigned to ^{13}CO, and m/z 45 is ascribed to the unconverted ^{13}CO$_2$. This experiment suggested that CO$_2$ is indeed the carbon source of CO for photocatalytic reduction reaction. It can be

deduced that the absorbed ^{13}CO$_2$ gas on the surface of as-prepared samples was photocatalyzed into ^{13}CO during the photoreaction, ruling out the possibility of produced CO from the organics in the system or on the surface of photocatalyst.

The CO$_2$ adsorption ability over the as-prepared samples was measured at 30 °C that is similar to the test temperature of CO$_2$ photoreduction experiment. As shown in Fig. S18, the adsorption volume of CO$_2$ of all the samples increases along with the increase of partial pressure, and the CO$_2$ capture performance of all the CN-x samples is higher than that of pure g-C$_3$N$_4$, because of the small specific surface area and insufficient reactive sites of bulk g-C$_3$N$_4$. CN-2 possesses the highest adsorption capacity with 3.36 cm^3/g at 1.5 kPa, which should be owing to the co-existence of the pore walls and porous inner-cores. Unlike the linear increase in physical adsorption, the adsorption capacity increases rapidly with CO$_2$ partial pressure increases. This conforms to the characteristics of chemical adsorption where the adsorption capacity is mainly proportional to the number of adsorption sites and is less dependent on the pressure of the adsorbate.

To reveal the mechanism of the enhanced photocatalytic activity, the surface charge transfer efficiency (η_{trans}) of the samples was measured, and the results are shown in Fig. 4a and b. η_{trans} can be obtained by Eq. (1), with the addition of a fast electron scavenger, methylviologen dichloride (MVCl$_2$), to the electrolyte [46–48]:

$$J_{H2O} = J_{max} \cdot \eta_{abs} \cdot \eta_{sep} \cdot \eta_{trans}, \tag{1}$$

where J_{H2O} and J_{max} are the measured and theoretical maximum photocurrent in the absence of an electron scavenger, respectively; η_{abs} is the light absorption efficiency; η_{sep} is the charge separation efficiency inside the photoanode; and η_{trans} is surface charge transfer efficiency of the photoanode.

In the presence of electron scavenger MV^{2+}, the surface charge transfer is very fast, and $\eta_{trans} \approx 100\%$. The photocurrent can be expressed as:

$$J_{MV^{2+}} = J_{max} \cdot \eta_{abs} \cdot \eta_{sep}. \tag{2}$$

Since the addition of MV^{2+} did not change the light absorption, the pH, $\eta_{sep} \cdot J_{max}$, η_{abs}, and η_{sep} are unaltered for both J_{H2O} and $J_{MV^{2+}}$. Therefore, the surface transfer efficiency can be calculated by comparing the photocurrent from water and the MV^{2+} reduction:

$$\eta_{trans} = J_{H2O}/J_{MV^{2+}}. \tag{3}$$

With the addition of MV^{2+}, the photocurrent density of the bulk g-C$_3$N$_4$ increases from 0.65 to 1.66 10^{-7} A cm^{-2}, while that of CN-2 increases from 2.98 to 5.83 10^{-7} A cm^{-2}. This increment is ascribed to the easier reduction of MV^{2+} than that of water molecules. The η_{trans} of g-C$_3$N$_4$ and CN-2 are calculated to be 39.1% and 51.1%, respectively, revealing that the PTYS CN-2 shows much faster charge transfer efficiency than bulk g-C$_3$N$_4$. This should be due to the shorter carrier diffusion distance of porous structure of PTYS CN-2 with tight interface between the inner nanorod and outer shell, enabling faster electron injection into the redox pair [49,50].

Determining the density of charge carriers helps to understand the mechanism of photocatalytic activity enhancement of CN-2. When adding the fast electron acceptor MV^{2+}, the photocurrent onset potential in a voltammogram reflects the quasi-Fermi-level of majority carriers. Since there is hardly any over-potential for the reduction of MV^{2+}, charge carriers can migrate to the external circuit for photocurrent generation once the applied bias reaches the quasi-Fermi-level [46–48]. As shown in Fig. 4c, the potentials of CN-1 (−0.333 V versus RHE), CN-2 (−0.307 V versus RHE), and CN-3 (−0.333 V versus RHE) are 0.006, 0.032, and 0.006 V more positive than that of bulk g-C$_3$N$_4$ (−0.339 V versus RHE) respectively. In the quasi-Fermi-level, the carrier density difference between CN-x and g-C$_3$N$_4$ can be calculated according to the Nernst equation [46–48]:

$$E_{f1} - E_{f2} = k.T.\ln(N_{f1}/N_{f2})/e, \tag{4}$$
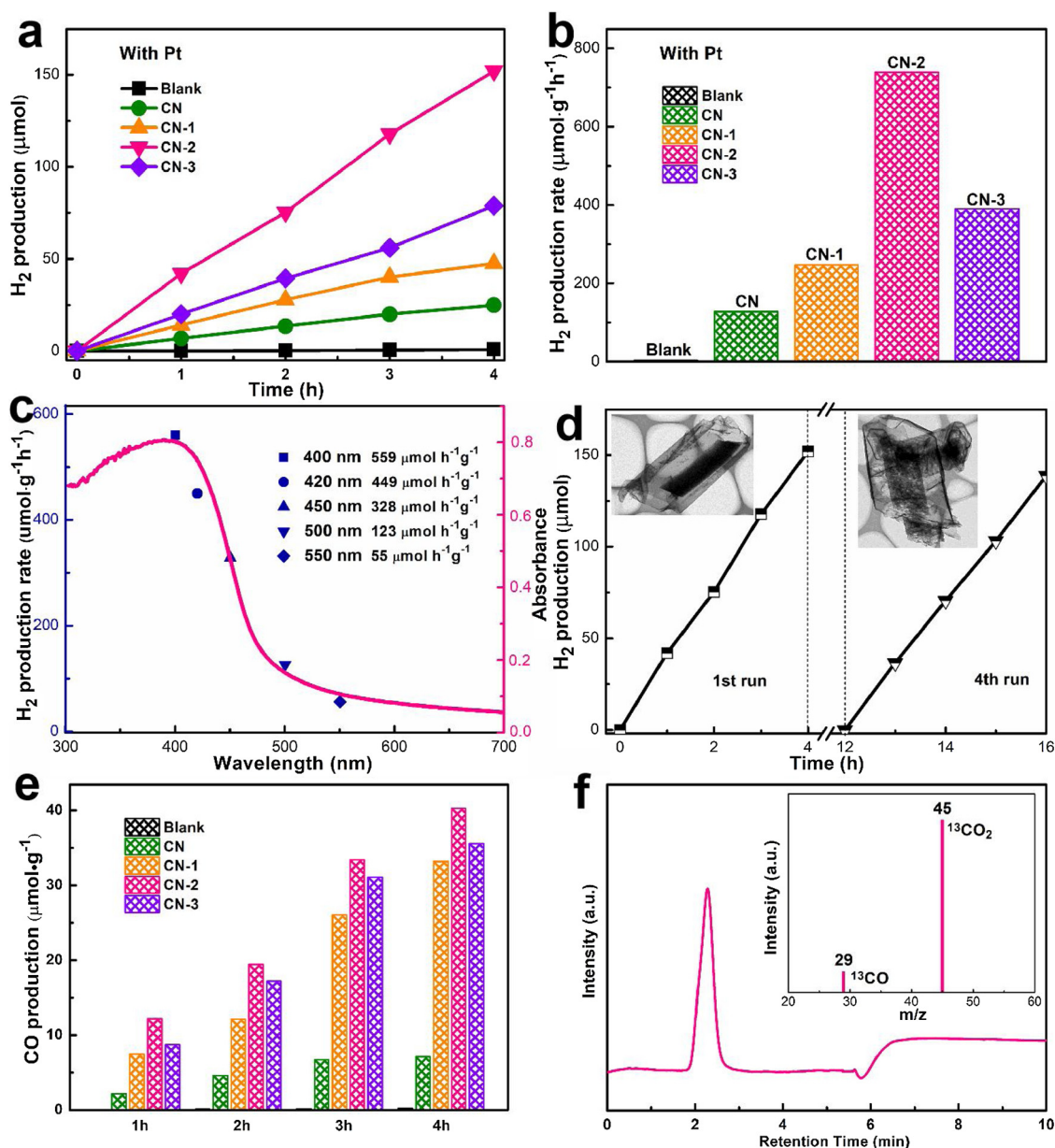
Fig. 3. a) Photocatalytic H_2 production curves, and b) H_2 production rate over pure CN and CN-x samples with loading Pt nanoparticles; c) The wavelength-dependent H_2 production rate for CN-2; d) Stability tests for photocatalytic H_2 production and the relative TEM images (insert) of CN-2; e) CO production rates over pure CN and CN-x samples; f) GC and MS (m/z = 29) curves (insert) over CN-2 with purging ^{13}CO.

where E_{f1} and N_{f1} are the quasi-Fermi-level and the carrier density at the Fermi level of sample 1, respectively; E_{f2} and N_{f2} are the corresponding values of sample 2; k is Boltzmann's constant; T is the temperature; and e is the elementary charge. The 0.006 V and 0.032 V shifts then correspond to 1.3 and 3.5 times higher carrier densities respectively in CN-1, CN-3, and CN-2, which is beneficial to photocatalytic water splitting.

Surface photovoltage (SPV) spectra of bulk CN and CN-*x* were measured to investigate the surface charge potential. From Fig. 4d, the gradually increased SPV response in the range of 310–450 nm is observed in the sequence of CN < CN-1 < CN-3 < CN-2, demonstrating that PTYS CN-2 has the largest bulk charge separation degree followed by the sample CN-3 [51,52]. Besides, it is worth noting that PSYS CN-3 exhibits a higher SPV signal intensity than CN-1, suggesting that the presence of inner rods is beneficial to the charge separation. Photoluminescence (PL) is herein employed to survey the recombination rate of electrons and holes. PTYS CN-2 shows the lowest PL emission

intensity (Fig. 4e), which revealed the most suppressed radiative recombination of CN-2 [53], consistent with the above photocurrent and SPV results. CN-3 delivers a much lower PL intensity than CN and CN-1, further confirming the positive role of inner rods in charge separation.

Time-resolved fluorescence decay spectra were also collected to investigate the charge recombination dynamics of the samples (Fig. 4f), and the lifetime (τ) of CN, CN-1, CN-2, and CN-3 were 3.065, 2.438, 2.211, and 2.432 ns, respectively. The shortest lifetime observed for CN-2 indicates the most efficient separation of electrons and holes, which is attributed to the fastest capture by reactive substrates to drive the redox reactions [54]. This is vital to understand the highly enhanced photocatalytic activity of CN-*x*, especially the PTYS CN-2. Electrochemical impedance spectroscopy (EIS) revealed that the arc radii of the Nyquist plots for all CN-*x* samples were smaller than that of pristine g-C_3N_4 (Fig. S19) with the smallest one for CN-2, implying that the CN-2 sample possesses the lowest interfacial charge-transfer resistance [55,56]. The above photoelectric and photelectrochemical
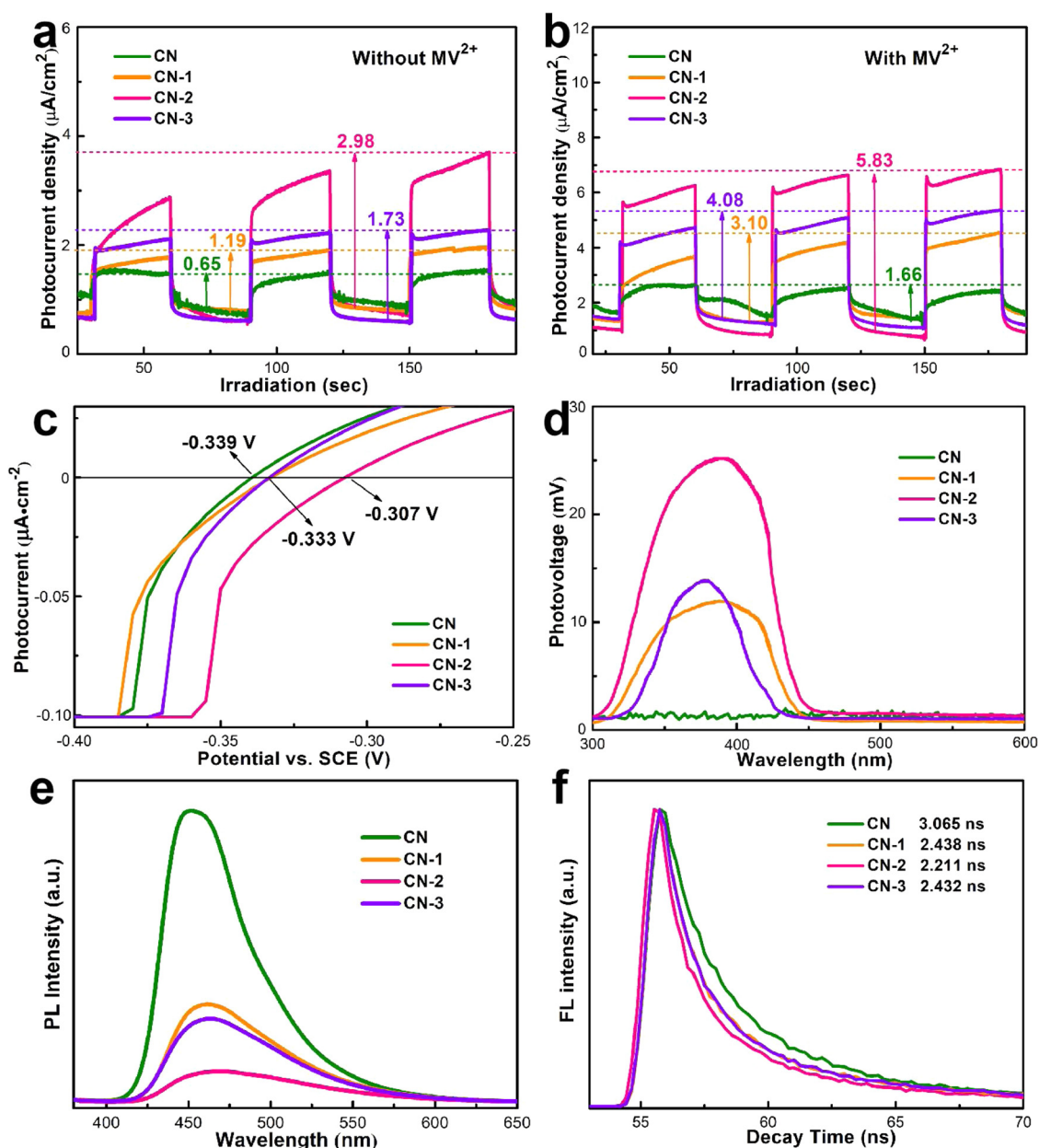
Fig. 4. Photocurrent density of CN and CN-2 under visible light (λ > 420 nm) in electrolyte of Na_2SO_4 [0.1 M] a) with and b) without addition of 0.001 M methylviologen dichloride ($MVCl_2$). c) Voltammograms of CN and CN-x under visible light (λ > 420 nm) in electrolyte of Na_2SO_4 [0.1 M] with 0.001 M $MVCl_2$. d) Surface photovoltage spectra, e) Photoluminescence spectra, and f) Time-resolved fluorescence spectra of CN and CN-x (E_x = 368 nm).

results show that the porous tubular structure consumedly enhances the separation/transfer of photogenerated charge carriers and depresses the recombination, and the inner rods can further strengthen the charge separation.

To provide a deep insight into the greatly enhanced photocatalytic H_2 evolution ability of porous tubular yolk-shell g-C_3N_4, the reactive sites of CN-2 for photo-reduction were investigated by Pt photo-deposition. As shown in Fig. 5a–d, Pt nanoparticles are uniformly dispersed on the outer walls of the CN-2 tubes. In particular, Pt nanoparticles are also found over the inner rods, demonstrating that both the outer walls and inner rods serve as the reactive sites for photo-reduction (Pt^{2+} + 2e⁻ → Pt). It suggests that abundant photogenerated electrons would be transferred to the outer walls and inner rods to participate in the photocatalytic H_2 evolution reaction. The detection of Cl and Cu is due to the precursor of $H_2PtCl_6\cdot 6H_2O$ and copper net in the photo-deposition and TEM measurement process (Fig. 5e), respectively. Based on the above analysis, the efficient photocatalytic H_2 production

activity of PTYS CN-2 is summarized as illustrated in Fig. 5f and in the following: (1) The mesopores on the outer shells and inner rods of CN-2 could enable a longer travel distance of light inside CN-2 through multiple scatterings and reflections, allowing it to absorb more visible light. (2) The porous tubular yolk-shell structure dramatically facilitates the separation and transport of photogenerated charge carriers of g-C_3N_4 and prohibits its recombination. (3) The rich reactive sites distributed over the outer walls and inner rods of PTYS CN-2 greatly benefit the reduction reaction of H^+/H_2O into H_2 and CO_2 into CO by abundant photogenerated electrons. Owing to the above merits, the porous tubular yolk-shell g-C_3N_4 exhibits a substantially enhanced photocatalytic activity H_2 production and CO_2 reduction.

4. Conclusions

In summary, we first prepare hexagonal prismatic melamine crystals as the precursor of g-C_3N_4 by hydrothermal re-crystallization with the
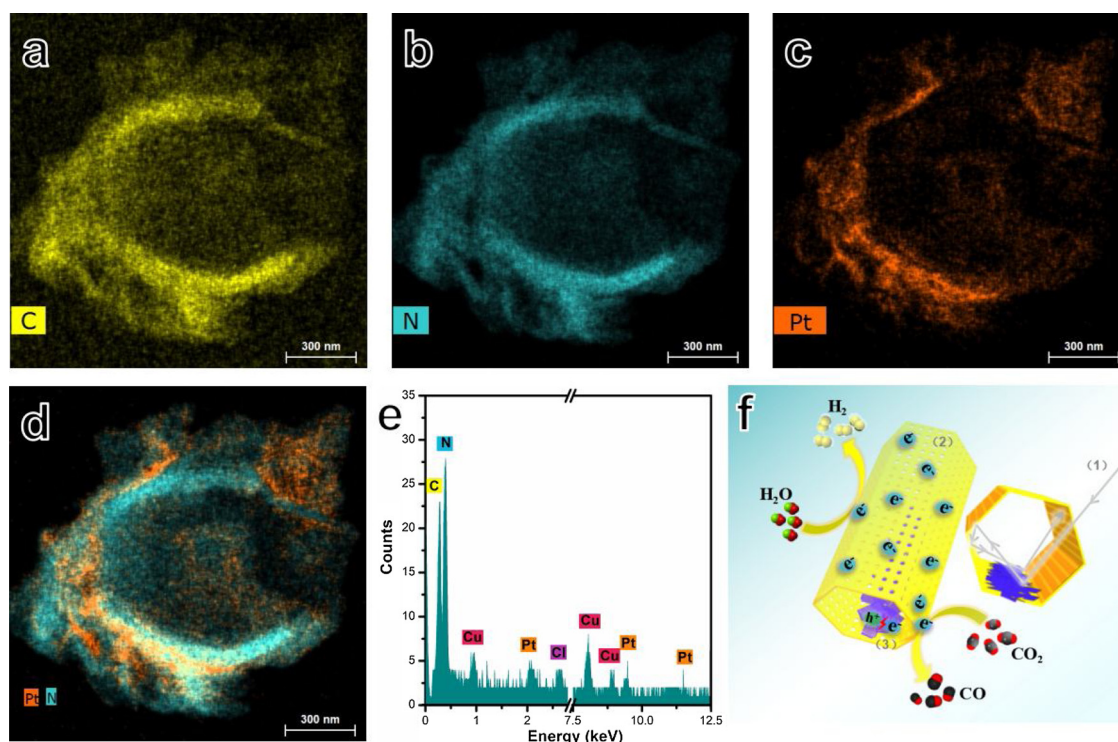
Fig. 5. TEM EDX mapping a) C, b) N, c) Pt, d) Pt and N of PTYS CN-2. e) TEM EDX of PTYS CN-2. f) The photocatalytic mechanism of the PTYS CN-2.

assistance of large vapour pressure derived from urea solution. The well-defined melamine crystals can also be obtained by replacing urea with other decomposable ammonium salts for providing gas pressure. After calcination of hexagonal prismatic melamine, three novel tubular-structured g-C_3N_4, including porous tubular (PT) g-C_3N_4, porous tubular yolk-shell (PTYS) g-C_3N_4, and porous split yolk-shell (PSYS) g-C_3N_4, are finally obtained. All the three novel structured g-C_3N_4 own enlarged specific surface area, enhanced photoabsorption and facilitated charges separation and transfer, resulting in their improved photocatalytic performance. Particularly, both the porous outer walls and inner cores of PTYS CN-2 consist of substantial reductive reactive sites, which greatly contribute to its highest photoreduction activity with a high H_2 evolution AQE of 11.8% at 420 nm and a superior CO production rate from CO_2 reduction (5.6-fold increase). This work opens the opportunity for fabrication of novel nano-architectures as a high-performance photocatalytic system for energetic applications.

Acknowledgment

Appendix A. Supplementary data

Supplementary material related to this article can be found, in the online version, at doi:https://doi.org/10.1016/j.apcatb.2019.04.036.

References

[1] W.G. Tu, Y. Zhou, Z.G. Zou, Photocatalytic conversion of CO_2 into renewable hydrocarbon fuels: state-of-the-art accomplishment, challenges, and prospects, Adv. Mater. 26 (2014) 4607–4626.

[2] W.G. Tu, Y. Xu, J.J. Wang, B.W. Zhang, T.H. Zhou, S.M. Yin, S.Y. Wu, C.M. Li, Y.Z. Huang, Y. Zhou, Z.G. Zou, J. Robertson, M. Kraft, R. Xu, Investigating the role of tunable nitrogen vacancies in graphitic carbon nitride nanosheets for efficient visible-light-driven H_2 evolution and CO_2 reduction, ACS Sustain. Chem. Eng. 5

(2017) 7260–7268.

[3] X.C. Wang, K. Maeda, A. Thomas, K. Takanabe, G.J. Xin, M.A. Carlsson, A metal-free polymeric photocatalyst for hydrogen production from water under visible light, Nat. Mater. 8 (2009) 76–80.

[4] Y. Wang, X.C. Wang, M. Antonietti, Polymeric graphitic carbon nitride as a heterogeneous organocatalyst: from photochemistry to multipurpose catalysis to sustainable chemistry, Angew. Chem. Int. Ed. 51 (2012) 68–89.

[5] Y. You, S.B. Wang, K. Xiao, T.Y. Ma, Y.H. Zhang, H.W. Huang, Z-scheme g-C_3N_4/Bi_4NbO_8Cl heterojunction for enhanced photocatalytic hydrogen production, ACS Sustain. Chem. Eng. 6 (2018) 16219–16227.

[6] S.C. Yan, Z.S. Li, Photodegradation performance of g-C_3N_4 fabricated by directly heating melamine, Langmuir 25 (2009) 10397–10401.

[7] F. Dong, L.W. Wu, Y.J. Sun, M. Fu, Z.B. Wu, S.C. Lee, Efficient synthesis of polymeric g-C_3N_4 layered materials as novel efficient visible light driven photocatalysts, J. Mater. Chem. 21 (2011) 15171–15174.

[8] M. Mousavi, A. Habibi-Yangjeh, Decoration of Fe_3O_4 and $CoWO_4$nanoparticles over graphitic carbon nitride: novel visible-light-responsive photocatalysts with exceptional photocatalytic performances, Mater. Res. Bull. 105 (2018) 159–171.

[9] Y.Y. Kang, Y.Q. Yang, L.C. Yin, X.D. Kang, L.Z. Wang, G. Liu, H.M. Cheng, Selective breaking of hydrogen bonds of layered carbon nitride for visible light photocatalysis, Adv. Mater. 28 (2016) 6471–6477.

[10] X.B. Chen, C. Li, M. Gratzel, R. Kostecki, S.S. Mao, Nanomaterials for renewable energy production and storage, Chem. Soc. Rev. 41 (2012) 7909–7937.

[11] F. Chen, H.W. Huang, L. Guo, Y.H. Zhang, T.Y. Ma, The role of polarization in photocatalysis, Angew. Chem. Int. Ed. (2019), https://doi.org/10.1002/anie.201901361.

[12] R. Kuriki, K. Sekizawa, O. Ishitani, K. Maeda, Visible-light-driven CO_2 reduction with carbon nitride: enhancing the activity of ruthenium catalysts, Angew. Chem. Int. Ed. 54 (2015) 2406–2409.

[13] M. Mousavi, A. Habibi-Yangjeh, Integration of $NiWO_4$ and Fe_3O_4 with graphitic carbon nitride to fabricate novel magnetically recoverable visible-light-driven photocatalysts, J. Mater. Sci. 53 (2018) 9046–9063.

[14] S. Asadzadeh-Khaneghah, A. Habibi-Yangjeh, K. Yubuta, Novel g-C_3N_4 nanosheets/CDs/BiOCl photocatalysts with exceptional activity under visible light, J. Am. Ceram. Soc. 102 (2019) 1435–1453.

[15] H.W. Huang, S.C. Tu, C. Zeng, T.R. Zhang, A.H. Reshak, Y.H. Zhang, Macroscopic polarization enhancement promoting photo- and piezoelectric-induced charge separation and molecular oxygen activation, Angew. Chem. Int. Ed. 56 (2017) 11860–11864.

[16] X.B. Chen, S.H. Shen, L.J. Guo, S.S. Mao, Semiconductor-based photocatalytic hydrogen generation, Chem. Rev. 110 (2010) 6503–6570.

[17] H. Diarmand-Khalilabad, A. Habibi-Yangjeh, D. Seifzadeh, S. Asadzadeh-Khaneghah, E. Vesali-Kermani, g-C3N4 nanosheets decorated with carbon dots and CdS nanoparticles: novel nanocomposites with excellent nitrogen photofixation ability under simulated solar irradiation, Ceram. Int. 45 (2019) 2542–2555.

[18] M. Mousavi, A. Habibi-Yangjeh, D. Seifzadeh, Novel ternary g-C_3N_4/Fe_3O_4/$MnWO_4$ nanocomposites: synthesis, characterization, and visible-light photocatalytic performance for environmental purposes, J. Mater. Sci. Technol. 34 (2018)

1638–1651.

[19] G.J.A.A. Soler-Illia, C. Sanchez, B. Lebeau, J. Patarin, Chemical strategies to design textured materials: from microporous and mesoporous oxides to nanonetworks and hierarchical structures, Chem. Rev. 102 (2002) 4093–4138.

[20] J.D. Xiao, Y.B. Xie, F. Nawaz, Y.X. Wang, P.H. Du, H.B. Cao, Dramatic coupling of visible light with ozone on honeycomb-like porous g-C$_3$N$_4$ towards superior oxidation of water pollutants, Appl. Catal. B 183 (2016) 417–425.

[21] H.J. Yu, L. Shang, T. Bian, R. Shi, G.I.N. Waterhouse, Y.F. Zhao, C. Zhou, L.Z. Wu, C.H. Tung, T.R. Zhang, Nitrogen-doped porous carbon nanosheets templated from g-C$_3$N$_4$ as metal-free electrocatalysts for efficient oxygen reduction reaction, Adv. Mater. 28 (2016) 5080–5086.

[22] Z.W. Tong, D. Yang, J.F. Shi, Y.H. Nan, Y.Y. Sun, Z.Y. Jiang, Three-dimensional porous aerogel constructed by g-C$_3$N$_4$ and graphene oxide nanosheets with excellent visible-light photocatalytic performance, ACS Appl. Mater. Interface 7 (2015) 25693–25701.

[23] Z.F. Huang, J.J. Song, L. Pan, Z.M. Wang, X.Q. Zhang, J.J. Zou, W.B. Mi, X.W. Zhang, L. Wang, Carbon nitride with simultaneous porous network and O-doping for efficient solar-energy-driven hydrogen evolution, Nano Energy 12 (2015) 646–656.

[24] S.E. Guo, Z.P. Deng, M.X. Li, B.J. Jiang, C.G. Tian, Q.J. Pan, H.G. Fu, Phosphorus-doped carbon nitride tubes with a layered micro-nanostructure for enhanced visible-light photocatalytic hydrogen evolution, Angew. Chem. Int. Ed. 55 (2016) 1830–1834.

[25] N. Tian, H.W. Huang, Y. He, Y.X. Guo, T.R. Zhang, Y.H. Zhang, Mediator-free direct Z-scheme photocatalytic system: BiVO$_4$/g-C$_3$N$_4$ organic-inorganic hybrid photocatalyst with highly efficient visible-light-induced photocatalytic activity, Dalton Trans. 44 (2015) 4297–4307.

[26] C.Y. Liu, H.W. Huang, L.Q. Ye, S.X. Yu, N. Tian, X. Du, T.R. Zhang, Y.H. Zhang, Intermediate-mediated strategy to horn-like hollow mesoporous ultrathin g-C$_3$N$_4$ tube with spatial anisotropic charge separation for superior photocatalytic H$_2$ evolution, Nano Energy 41 (2017) 738–748.

[27] H.W. Huang, K. Xiao, N. Tian, F. Dong, T.R. Zhang, X. Du, Y.H. Zhang, Template-free precursor-surface-etching route to porous, thin g-C$_3$N$_4$ nanosheets for enhancing photocatalytic reduction and oxidation activity, J. Mater. Chem. A Mater. Energy Sustain. 5 (2017) 17452–17463.

[28] C.Y. Liu, H.W. Huang, W. Cui, F. Dong, Y.H. Zhang, Band structure engineering and efficient charge transport in oxygen substituted g-C$_3$N$_4$ for superior photocatalytic hydrogen evolution, Appl. Catal. B 230 (2018) 115–124.

[29] J.H. Wang, C. Zhang, Y. Shen, Z. Zhou, J. Yu, Y. Li, W. Wei, S. Liu, Y. Zhang, Environment-friendly preparation of porous graphite-phase polymeric carbon nitride using calcium carbonate as templates, and enhanced photoelectrochemical activity, J. Mater. Chem. A Mater. Energy Sustain. 3 (2015) 5126–5131.

[30] T. Rodenas, I. Luz, G. Prieto, B. Seoane, H. Miro, A. Corma, F. Kapteijn, I.X.F.X. Llabres, J. Gascon, Metal-organic framework nanosheets in polymer composite materials for gas separation, Nat. Mater. 14 (2015) 48–55.

[31] T. Wang, X. Meng, P. Li, S. Ouyang, K. Chang, G. Liu, Z. Mei, J. Ye, Photoreduction of CO$_2$ over the well-crystallized ordered mesoporous TiO$_2$ with the confined space effect, Nano Energy 9 (2014) 50–60.

[32] R.J. Cumbest, Grain-boundary morphology and crystallography in recrystallized hornblende, Eur. J. Mineral. 3 (1991) 549–558.

[33] Y. Yazawa, T. Furuhara, T. Maki, Effect of matrix recrystallization on morphology, crystallography and coarsening behavior of vanadium carbide in austenite, Acta Mater. 52 (2004) 3727–3736.

[34] H.A. Ma, X. Jia, Q.L. Cui, Y.W. Pan, P.W. Zhu, B.B. Liu, H.J. Liu, X.C. Wang, J. Liu, G.T. Zou, Crystal structures of C$_3$N$_6$H$_6$ under high pressure, Chem. Phys. Lett. 368 (2003) 668–672.

[35] N. Tian, Y.H. Zhang, X.W. Li, K. Xiao, X. Du, F. Dong, G.I.N. Waterhouse, T.R. Zhang, H.W. Huang, Precursor-reforming protocol to 3D mesoporous g-C$_3$N$_4$ established by ultrathin self-doped nanosheets for superior hydrogen evolution, Nano Energy 38 (2017) 72–81.

[36] H.J. Yu, R. Shi, Y.X. Zhao, T. Bian, Y.F. Zhao, C. Zhou, G.I.N. Waterhouse, L.Z. Wu, C.H. Tung, T.R. Zhang, Alkali-assisted synthesis of nitrogen deficient graphitic carbon nitride with tunable band structures for efficient visible-light-driven hydrogen evolution, Adv. Mater. 29 (2017) 1605148.

[37] Y.X. Li, S.X. Ouyang, H. Xu, X. Wang, Y.P. Bi, Y.F. Zhang, J.H. Ye, Constructing solid-gas-interfacial fenton reaction over alkalinized-C$_3$N$_4$ photocatalyst to achieve apparent quantum yield of 49% at 420 nm, J. Am. Chem. Soc. 138 (2016) 13289–13297.

[38] W. Ho, Z.Z. Zhang, W. Lin, S.P. Huang, X.W. Zhang, X.X. Wang, Y. Huang, Copolymerization with 2,4,6-triaminopyrimidine for the rolling-up the layer structure, tunable electronic properties, and photocatalysis of g-C$_3$N4, ACS Appl. Mater. Interface 7 (2015) 5497–5505.

[39] T.Y. Ma, S. Dai, M. Jaroniec, S.Z. Qiao, Graphitic carbon nitride nanosheet-carbon nanotube three-dimensional porous composites as high-performance oxygen evolution electrocatalysts, Angew. Chem. Int. Ed. 126 (2014) 7409–7413.

[40] G.H. Dong, L.P. Yang, F. Wang, L. Zang, C.Y. Wang, Removal of nitric oxide through visible light photocatalysis by g-C$_3$N$_4$ modified with perylene imides, ACS Catal. 6 (2016) 6511–6519.

[41] S. Martha, A. Nashim, K.M. Parida, Facile synthesis of highly active g-C$_3$N$_4$ for efficient hydrogen production under visible light, J. Mater. Chem. A Mater. Energy Sustain. 1 (2013) 7816–7824.

[42] Q.L. Tay, P. Kanhere, C.F. Ng, S. Chen, S. Chakraborty, A.C.H. Huan, T.C. Sum, R. Ahuja, Z. Chen, Defect engineered g-C$_3$N$_4$ for efficient visible light photocatalytic hydrogen production, Chem. Mater. 27 (2015) 4930–4933.

[43] H.W. Huang, K. Xiao, T.R. Zhang, F. Dong, Y.H. Zhang, Rational design on 3D hierarchical bismuth oxyiodides via in situ self-template phase transformation and phase-junction construction for optimizing photocatalysis against diverse contaminants, Appl. Catal. B: Environ. 203 (2017) 879–888.

[44] J.S. Zhang, F.S. Guo, X.C. Wang, An optimized and general synthetic strategy for fabrication of polymeric carbon nitride nanoarchitectures, Adv. Funct. Mater. 23 (2013) 3008–3018.

[45] K. Kailasam, J.D. Epping, A. Thomas, S. Losse, H. Junge, Mesoporous carbon nitride-silica composites by a combined sol–gel/thermal condensation approach and their application as photocatalysts, Energy Environ. Sci. 4 (2011) 4668–4674.

[46] S. Patnaik, S. Martha, S. Acharya, K. Parida, An overview of the modification of g-C3N$_4$ with high carbon containing materials for photocatalytic applications, Inorg. Chem. Front. 3 (2016) 336–347.

[47] W. Liu, M.L. Wang, C.X. Xu, S.F. Chen, X.L. Fu, Significantly enhanced visible-light photocatalytic activity of g-C$_3$N$_4$ via ZnO modification and the mechanism study, J. Mol. Catal. A Chem. 368 (2015) 9–15.

[48] R.C. Pawar, S. Kang, S.H. Ahn, C.S. Lee, Gold nanoparticle modified graphitic carbon nitride/multi-walled carbon nanotube (g-C$_3$N$_4$/CNTs/Au) hybrid photocatalysts for effective water splitting and degradation, RSC Adv. 5 (2015) 24281–24292.

[49] J. Liu, J.H. Huang, H. Zhou, M. Antonietti, Uniform graphitic carbon nitride nanorod for efficient photocatalytic hydrogen evolution and sustained photoenzymatic catalysis, ACS Appl. Mater. Interface 6 (2014) 8434–8440.

[50] X.J. Bai, L. Wang, R.L. Zong, Y.F. Zhu, Photocatalytic activity enhanced via g-C$_3$N$_4$ nanoplates to nanorods, J. Phys. Chem. C 117 (2013) 9952–9961.

[51] F. Chen, H.W. Huang, L.Q. Ye, T.R. Zhang, Y.H. Zhang, X.P. Han, T.Y. Ma, Thickness-dependent facet junction control of layered BiOIO$_3$ single crystals for highly efficient CO$_2$ photoreduction, Adv. Funct. Mater. 28 (2018) 1804284.

[52] Z.Y. Liu, D.D. Sun, P. Guo, J.O. Leckie, An efficient bicomponent TiO$_2$/SnO$_2$ nanofiber photocatalyst fabricated by electrospinning with a side-by-side dual spinneret method, Nano Lett. 7 (2007) 1081–1085.

[53] H.W. Huang, X.W. Li, J.J. Wang, F. Dong, P.K. Chu, T.R. Zhang, Y.H. Zhang, Anionic group self-doping as a promising strategy: band-gap engineering and multi-functional applications of high-performance CO$_3^{2-}$ doped Bi$_2$O$_2$CO$_3$, ACS Catal. 5 (2015) 4094–4103.

[54] Y.X. Li, H. Xu, S.X. Ouyang, D. Lu, X. Wang, D.F. Wang, J.H. Ye, In situ surface alkalinized g-C$_3$N$_4$ toward enhancement of photocatalytic H$_2$ evolution under visible-light irradiation, J. Mater. Chem. A Mater. Energy Sustain. 4 (2016) 2943–2950.

[55] H.J. Yu, J.Y. Li, Y.H. Zhang, S.Q. Yang, K.L. Han, F. Dong, T.Y. Ma, H.W. Huang, Three-in-one oxygen vacancy: whole visible-spectrum absorption, efficient charge separation and surface site activation for robust CO$_2$ photoreduction, Angew. Chem. Int. Ed. 58 (2019) 3880–3884.

[56] H.W. Huang, K. Xiao, Y. He, T.R. Zhang, F. Dong, X. Du, Y.H. Zhang, In situ assembly of BiOI@Bi$_{12}$O$_{17}$Cl$_2$p-n junction: charge induced unique front-lateral surfaces coupling heterostructure with high exposure of BiOI {001} active facets for robust and nonselective photocatalysis, Appl. Catal. B: Environ. 199 (2016) 75–86.